

# The GLUEX Start Counter Detector

E. Pooser<sup>a,b</sup>, F. Barbosa<sup>a</sup>, W. Boeglin<sup>b,\*</sup>, C. Hutton<sup>a</sup>, M. Ito<sup>a</sup>, M. Kamel<sup>b</sup>, P. Khetarpal<sup>b</sup>, A. LLodra<sup>b</sup>, N. Sandoval<sup>a</sup>, S. Taylor<sup>a</sup>, C. Yero<sup>b</sup>, T. Whitlatch<sup>a</sup>, S. Worthington<sup>a</sup>, B. Zihlmann<sup>a</sup>

<sup>a</sup>*Thomas Jefferson National Accelerator Facility, Newport News, VA 23606, USA*

<sup>b</sup>*Florida International University, Miami, FL, 33199, USA*

---

## Abstract

The design, fabrication, calibration, and performance of the GLUEX Start Counter detector is described. The Start Counter detector was designed to operate at photon intensities of up to  $10^8 \gamma/\text{s}$  in the coherent peak and provides a timing resolution of  $\approx 250 \text{ ps}$  thus providing successful identification of the electron beam buckets to more than 99% accuracy. Furthermore, the Start Counter detector provides excellent solid angle coverage,  $\sim 90\%$  of  $4\pi$  hermeticity, a high degree of segmentation for background rejection, and is utilized in the level 1 trigger for the experiment. It consists of a cylindrical array of 30 thin scintillators with pointed ends that bend towards the beam at the downstream end. Magnetic field insensitive silicon photomultiplier detectors were selected as the readout system.

*Keywords:* GLUEX, Flash 250 MHz ADC, F1 TDC, Plastic Scintillator, Silicon Photomultiplier, Multi-Pixel Photon Counter, Time of Flight, Trigger, Particle Identification, Polishing Scintillators

---

## 1. Introduction

The GLUEX experiment, staged in Hall D at the Thomas Jefferson National Accelerator Facility (TJNAF), primarily aims to study the rich spectrum of photo-produced mesons with unprecedented statistics. The coherent bremsstrahlung technique is implemented to produce a linearly polarized photon beam incident on a liquid  $H_2$  target. A Start Counter detector was fabricated to properly identify the accelerator electron beam buckets and to provide accurate timing information.

## 2. Design

In this section we discuss the details of the GLUEX Start Counter design. The general engineering specifics pertaining to the scintillators, support structure, detector readout system and electronics are discussed.

### 2.1. Overview

The Start Counter (ST) detector, seen in Fig. 1, surrounds a 30 cm long super cooled liquid  $H_2$  target while providing  $\sim 90\%$  of  $4\pi$  solid angle coverage relative to the target center. The primary purpose of the ST detector is, in coincidence with the tagger, to properly identify the electron beam bucket associated with detected particles produced

---

\*Corresponding Author

Email address: [boeglinw@fiu.edu](mailto:boeglinw@fiu.edu) (W. Boeglin)

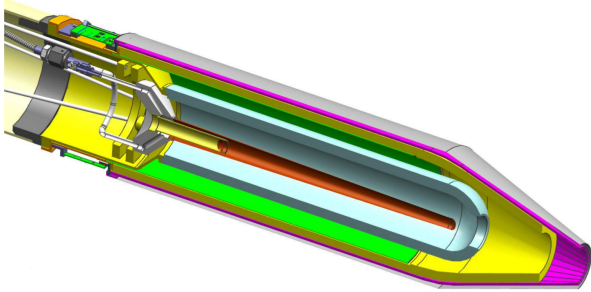


Figure 1: The GLUEX Start Counter mounted to the LH<sub>2</sub> target.

via linearly polarized photons incident on the target. It is designed to operate at tagged photon intensities of up to  $10^8 \gamma/\text{s}$  in the coherent peak. Moreover, the ST has a high degree of segmentation for background rejection, is utilized in particle identification, and is a primary component of the level 1 trigger of the GLUEX experiment during high luminosity running[1].

The ST detector consists of an array of 30 scintillators with pointed ends that bend towards the beam at the downstream end. EJ-200 scintilla-

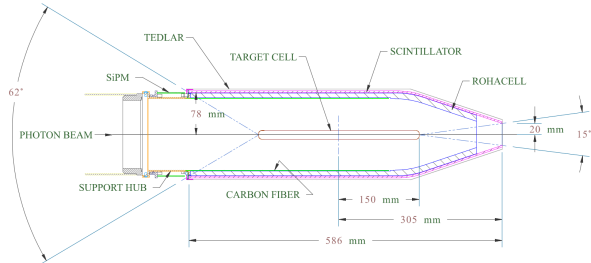


Figure 2: Cross section of the Start Counter detector.

tor material from Eljen Technology[2], which provides a decay time of 2.1 ns and a long attenuation length[3], was selected for this application. The amount of support structure material was kept to an absolute minimum in the active region of the detector and is made up of low density Rohacell[4].

Silicon Photomultiplier (SiPM) detectors were selected as the readout system. The detectors are not affected by the high magnetic field produced by the superconducting solenoid magnet. Moreover, the SiPMs were placed as close as possible to the upstream end of each scintillator element, thereby minimizing the loss of scintillation light[1].

## 2.2. Scintillator Paddles

Each individual paddle of the Start Counter was machined from a long, thin, polyvinyltoluene plastic EJ-200 scintillator bar that was diamond milled to be 600 mm in length, 3 mm thick, and  $20 \pm 2$  mm wide, by Eljen Technology. Each scintillator was bent around a highly polished aluminum drum by applying localized infrared heating to the bend region. The bent scintillator bars were then sent to McNeal Enterprises Inc.[5], a plastic fabrication company, where they were machined to the desired geometry illustrated in Fig. 3.

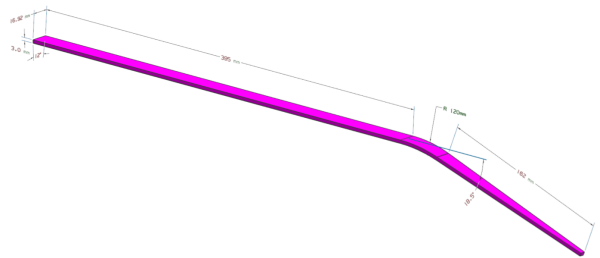


Figure 3: Start Counter single paddle geometry

The paddles consist of three sections and are described from the upstream to the downstream end of the target. The straight section is 39.5 cm in length while being oriented parallel to both the target cell and beamline.. The bend region is a  $18.5^\circ$  arc of radius 120 cm and is downstream of the straight section. The tapered nose region is

downstream of the target chamber and bends towards the beam line such that the tip of the nose is at a height of 2 cm above the beam line.

After the straight scintillator bar was bent to the desired geometry, the two flat surfaces that are oriented orthogonal to the wide, top and bottom, surfaces were cut at a 6° angle. During this process, the width of the top and bottom surfaces were machined to be 16.92 mm and 16.29 mm wide respectively. Thus, each of the paddles may be rotated 12° with respect to the paddle that preceded it so that they form a cylindrical shape with a conical end. This geometrical design for the ST increases solid angle coverage while minimizing multiple scattering.

### 2.3. Support Structure

The ST scintillator paddles are placed atop a low density Rohacell ( $\rho = 0.075 \text{ g/cm}^3$ ) foam support structure which envelopes the target vacuum chamber seen in Fig. 4. The Rohacell, which is 11 mm

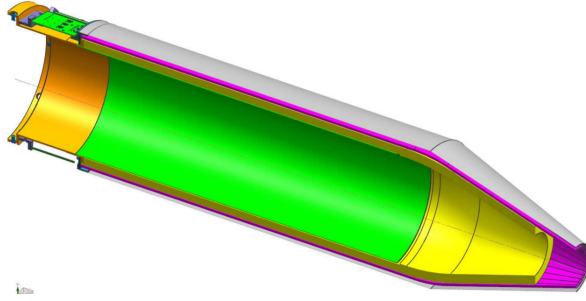


Figure 4: Cross section of the Start Counter detector

thick, is rigidly attached to the upstream support chassis and extends down the length of paddles however, not to include the last few centimeters of the conical nose section. Glued to the inner diameter of the Rohacell support structure are 3 layers of

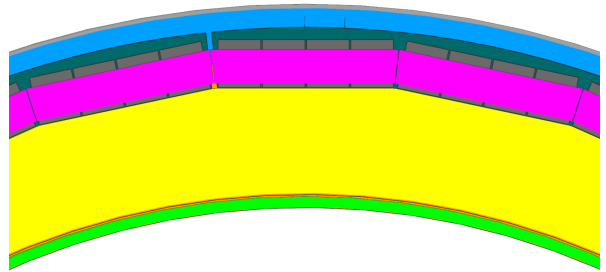


Figure 5: Composition of the Start Counter Materials.

carbon fiber ( $\rho = 1.523 \text{ g/cm}^3$ ) each of which are 650  $\mu\text{m}$  thick. A cross section of the ST can be seen in Fig. 4 where the carbon fiber is visible. The carbon fiber provides additional support during the assembly process as well as long term rigidity.

The various layers of material that comprise the ST support structure is illustrated in Fig. 5. In order to ensure that the detector was light-tight, a plastic collar was placed around the top of the SiPMs at the upstream end as seen in Fig. 5. The collar served as a lip to which a cylindrical sheet of black Tedlar was taped too. At the tip of the nose, a cone of Tedlar was then connected to the aforementioned cylindrical section. To make the downstream end of the ST light-tight, another cone of Tedlar was taped to the nose of the inner Rohacell support structure and then attached to the top Tedlar cone layer.

### 2.4. SiPM Readout Detectors

The selected readout for each scintillator bar is the magnetic field insensitive Hamamatsu S10931-050P surface mounted Multi-Pixel Photon Counters (MPPCs)[6]. An individual  $3 \times 3 \text{ mm}^2$  MPPC, also known as a SiPM, in the aforementioned configuration is comprised of 3600 individual,  $50 \times 50 \mu\text{m}^2$ ,

Avalanche Photo-Diode (APD) pixel counters operating in Geiger mode. The signal output from each SiPM is the total sum of the outputs from all 3600 APD pixels[7]. The scintillation light from an individual scintillator bar is collected by an array of four of these SiPMs.

The SiPM readout detectors are housed in a ceramic case which is surface mounted to a custom fabricated Printed Circuit Board (PCB). The PCB is held in a fixed position while being attached to the lip of the upstream chassis *via* two screws as illustrated in Fig. 6. The individual ST scintillators are coupled *via* an air gap ( $< 250\mu m$ ) to groups of four SiPMs set in a circular arrangement as can be seen in Fig. 6.



Figure 6: ST1 of Start Counter read out system. The ST1's are rigidly attached to the upstream support chassis. Approximately 72% of the scintillator light is collected at the upstream end.

### 2.5. Readout Electronics

The SiPMs reading out one individual paddle, are current summed prior to pre-amplification. The output of each preamp is then split; buffered for the Analog to Digital Converter (ADC) output, and amplified for the Time to Digital Converter (TDC) output by a factor five relative to the ADC. The ADC outputs are readout *via* JLab VME64x

250 MHz Flash ADC modules while the TDC outputs are input into JLab leading edge discriminators, followed by a high resolution 32 channel JLab VME64x F1TDC V2 module. Furthermore, each group of four SiPMs utilizes a thermocouple for temperature monitoring. There are 120 SiPMs in total, for a total of 30 pre-amplifier channels as seen Fig. 7.

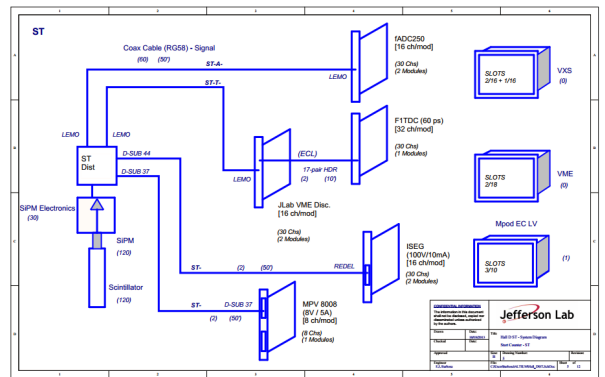


Figure 7: Start counter readout electronics diagram.

There are three components that comprise the ST detector readout system. The first component is the ST1 which holds 3 groups of 4 SiPMs as can be seen in Fig. 6. In order to mimic the geometry of the 30 paddle design one group of SiPM's is rotated by  $12^\circ$  relative to the central group, while the other adjacent group is rotated by  $-12^\circ$ . One ST1 unit will collect light from three paddles individually. The ST1 implements the current sum and bias distribution per group of 4 SiPMs. It also has a thermocouple for temperature monitoring.

The second component is the ST2, seen in Fig. 8, is a Printed Circuit Board (PCB) that houses the signal processing electronics of the readout system. It has 3 channels of pre-amplifiers, 3 buffers, and 3 factor five amplifiers. Furthermore, it has 3 bias



Figure 8: Fully assembled ST readout system.

distribution channels with individual temperature compensation *via* thermistors. The ST2 is attached to the ST1 *via* 90° hermaphroditic connector.

The third component of the readout system, the ST3 seen in Fig. 9, provides interface to the power and bias supplies. It also routes the ADC and TDC



Figure 9: Start counter ST3 readout system.

outputs as well as the thermocouple output. The ST3 connects to the ST2 *via* a signal cable assembly seen in Fig. 8 and Fig. 9. The ST3 is installed upstream of the Start Counter and next to the beam pipe.

### 3. GEANT4 Simulations

In this section, the Monte Carlo (MC) simulations that were conducted in order to better understand the performance and characteristics of scintillators machined to the nominal GLUEX Start Counter design are discussed. The MC studies were performed with the use of the tool-kit GEANT4 which simulates the passage of particles through matter [8]. Comparisons are made with the data observed in experiments conducted on the bench in Sec. 5.2 and with beam data in Sec. ??.

#### 3.1. Simulating a Simplified Model of the ST

As discussed in Sec. 2.2, the ST scintillator paddles have a unique geometry in which the nose section tapers in width as the paddles approach the beam line at the downstream end. This tapering effect results in a unique phenomenon in which the light output of the scintillator paddle begins to increase as the source moves further away from the readout detector. At first, this phenomenon is completely contrary to what one might expect. In the traditional sense when the source moves further away from the end being readout, the photons have a larger effective path length and thus, have an increased probability in being lost for detection. However, this is antithetical relative to what is observed on the bench and in experiment.

A primitive GEANT4 simulation was conducted to investigate the aforementioned phenomenon. For simplicity, only the two trapezoidal regions of a machined scintillator paddle were considered. Namely, the wide straight section and the tapered nose section which are illustrated in the GEANT4 event display seen in Fig. 10.

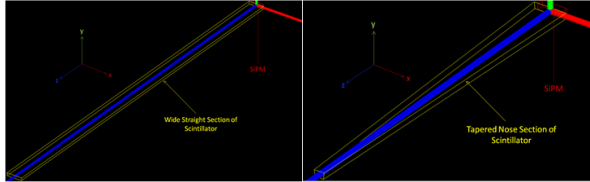


Figure 10: Simulated straight & nose section geometries. Shown is the GEANT4 event display. Left: wide straight section. Right: tapered nose section. The sections have been oriented such that they are in the same coordinate system as defined in HallD. The yellow lines are the scintillator boundaries, while the red lines are the boundaries of the SiPM.

The EJ-200 scintillator material ( $\rho = 1.023 \text{ g/cc}^3$ ,  $n = 1.58$ ) [3] was simulated with only one free parameter utilized to characterize the scintillator bar *i.e.*, the reflectivity of the  $G4LogicalSkinSurface$ , was set to 98% so there remained some finite probability that photons could be lost in the scintillator medium. Furthermore, the SiPM readout detector was placed at the upstream end of the two sections, seen in Fig. 10. Moreover, the SiPM was constructed as a  $G4SensitiveDetector$  made of Silicon with a 100% detection efficiency. The SiPM was constructed to have an active area of  $3 \times 12 \text{ mm}^2$  which is identical to the readout system described in Sec. 2.4.

In order to simulate a charged particle traversing through the scintillator medium resulting in the production of photons along its path through the material, optical photons were generated inside the volume of the simulated scintillator material. The scintillation yield was defined to be  $10,000 \gamma/\text{s}/1 \text{ MeV}$  [3]. For visual purposes, Fig. 11 shows 100 optical photons being produced at the

tip of the downstream end of the two sections of the simulated scintillator paddle.

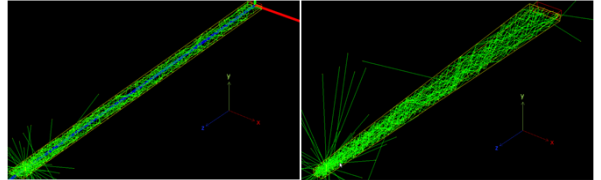


Figure 11: 100 Optical photons generated in the straight & nose sections. Left: wide straight section. Right: tapered nose section. The neon green lines are the paths of the optical photons. It is clear that some photons do in fact escape the scintillator medium, while others are collected in the simulated SiPM detector.

In order to sample the entirety of the two sections, 10,000 optical photons were generated at 16 different locations inside the medium of the scintillator. The photon energies ranged between 0.5–3.0

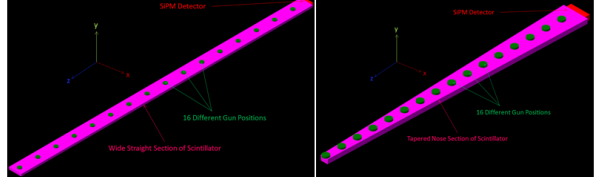


Figure 12: Optical photon gun locations along the straight & nose sections. Left: wide straight section. Right: tapered nose section. The magenta geometries indicate the scintillator boundaries of the two sections. The red box is the sensitive SiPM detector, and the green cylinders represent the location of the 16 optical photon gun locations. The locations of the source were chosen to be equal distances apart relative to each of the two sections.

eV [9] and were generated randomly in  $4\pi$  along a 3 mm path ( $y - \text{axis}$ ) in the scintillator medium. The path was oriented orthogonal to the wide surface of the scintillator. In essence, this simulates a charged particle traversing through the medium with a  $\theta_{track} = 90^\circ$  in hall coordinates. The num-

ber of photons collected by the SiPM at each of the 16 source locations is counted and correlated to the source location. The results can be seen in Fig. 13. From the data it is clear that the geom-

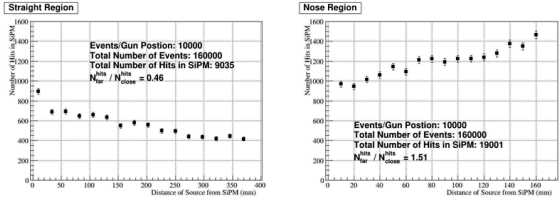


Figure 13: Simulation results for simplified two section scenario. The total number of photons which were collected by the SiPM detector at each of the 16 source locations is plotted against the sources distance from the sensitive detector. Left: wide straight section. Right: tapered nose section.

try of the nose section results in an improvement of light collection as the source moves further away from the readout detector. In fact, there is a factor  $\approx 1/2$  light loss observed in the straight section upon comparing the number of hits collected at the closest and furthest locations relative to the readout detector. However, there is factor  $\approx 3/2$  light gain observed in the nose region. These results are primarily due to the tapering trapezoidal geometry in the nose section. This phenomenon is not observed in the quasi-rectangular straight section as it exhibits a more conventional behavior. However, this behavior in the nose region is advantageous since the majority of forward going charged particles will traverse through the this region.

### 3.2. Simulating Machined Scintillator Geometry

Further simulations were conducted to simulate more realistically the effects of light collection that results from the ST scintillator geometry and optical surface quality. The ST scintillator geom-

etry was imported into GEANT4 from a Vectorworks CAD drawing utilizing the CADMesh utility [10] and is shown *via* the GEANT4 event display in Fig. 14. The SiPM was constructed as

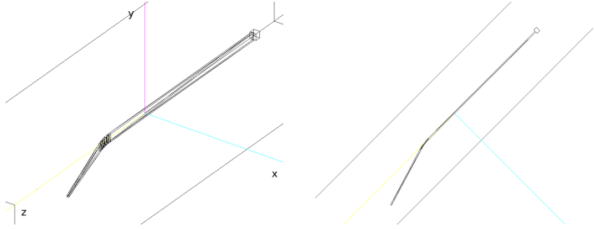


Figure 14: Scintillator geometry imported into GEANT4 utilizing CADMesh Utility. The scintillator is coupled to a SiPM detector. Left: isometric view. Right: top view. The tapering of the nose section is clearly visible.

a  $12 \times 12 \times 10$  mm $^3$  volume with a  $100 \mu\text{m}$  air gap between it and the wide end of the straight section. Furthermore, the volume surrounding the scintillator volume was air. The EJ-200 scintillator material, SiPM silicon detector, and optical photons were defined in an identical manner discussed in Sec. 3.1.

To simulate the imperfections of the scintillator surfaces due to manufacturing and machining, an optical surface “skin” was defined. The “skin” material was defined to be of they type “dielectric-dielectric” and made use of the UNIFIED physics model [11] to define an imperfect scintillator surface. Both the transmission efficiency and reflection parameters were implemented as free parameters to study their various effects on light transmission..

The UNIFIED model allows one to define the finish of the scintillator surface as *polished*, *ground*, or *unified* and is illustrated in Fig. 15 [11].

In the polished model, Fresnel reflection and refraction is assumed, where as the ground model al-

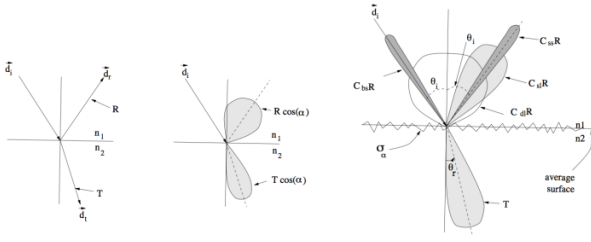


Figure 15: UNIFIED Model of scintillator surfaces. Left: Polar plot of the radiant intensity of the polished (left) and ground (right) models. Right: Polar plot of the radiant intensity in the UNIFIED model.

lows for Lambertian reflection, Fresnel refraction, backscattering, as well as spike and lobe reflections. The spike ( $C_{ss}$ ) reflection parameter assumes the optical photons are reflected as if the surface was a perfect mirror. The backscattering ( $C_{bs}$ ) reflection parameter assumes the photon is reflected in the same direction of incidence. The Lambertian ( $C_{dl}$ ) reflection parameter assumes that the photons are reflected corresponding to a Lambertian distribution. The lobe ( $C_{sl}$ ) reflection parameter assumes that the photons will reflect based on the orientation of the micro-facet on the scintillator surface, where  $\sigma_\alpha$  defined the standard deviation of the distribution of the micro-facets orientation [11]. One caveat of the aforementioned models is that they assume identical parameters for the entire optical surface [12].

As was done in section 3.1, 10,000 optical photons were generated in the scintillator medium every 2.5 cm and the number of hits collected in the SiPM were recorded. The results of these simulations are shown in Fig. 16. It is clear that if the transmission efficiency is increased while assuming a polished surface, the amount of light collected in the SiPM also increases as illustrated in Fig. 16. Simi-

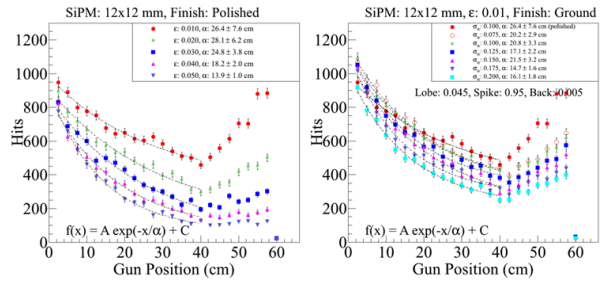


Figure 16: UNIFIED Model results. Left: polished model while varying the transmission efficiency. Right: ground model with varying  $\sigma_\alpha$  which characterizes the standard deviation of the surfaces micro-facet orientation.

larly, as the number of micro-facet orientations increase, meaning a more coarsely ground surface, the amount of light collection in the SiPM decreases. Moreover, in the instances where the surface quality of the machined scintillators are good, the phenomenon of light increase in the nose region as the source moves further from the readout detector is observed.

#### 4. Misalignment Studies

In order to protect both the active area of the SiPMs and the scintillator surface at the upstream end, the coupling distance between the two was required to be larger than zero. Similarly, during assembly the scintillator paddles were also shimmed radially such that the top edge of the scintillator was level with the top edge of the active area of the SiPM thereby maximizing light collection. In this section we discuss the relative coupling, as well as the subsequent effects regarding light collection and time resolution, between a machined scintillator paddle and a SiPM readout detector.

#### 4.1. Experimental Set-up

A custom fabricated test stand, further discussed in Sec. 5.2, and a polished scintillator machined to the nominal ST geometry, were utilized for these studies. The readout SiPM sat atop a Newport MT-XYZ (MT) compact dovetail XYZ linear translation stage[13] with three fine adjustment screws consisting of 80 threads per inch. Each knob for the three axes provides a translation of  $318 \mu\text{m}$  per rotation. For each location of the SiPM, the source and trigger PMT were located 24.5 cm downstream from the readout end.

To study the effects of the various horizontal (translations along the  $z$ -axis) coupling distances, the relative position of the active area of the SiPM and the top edge of the scintillator paddle, or vertical (translations along the  $y$ -axis) alignment, was required to be known prior too.

Utilizing an Edmund Optics complementary metal oxide semiconductor (CMOS) camera, and a reference ruler (seen in Fig. 17) the vertical alignment of the top edges of the SiPM and scintillator were measured with 0.025 mm accuracy. A micrometer was utilized in order to cross check the optical measurements and to provide absolute measurements of fixed distances in the experimental set-up. We have defined that at  $y = 0$  the SiPM and scintillator ( $z$ ) was set to a distance of 100  $\mu\text{m}$  and monitored closely during the vertical alignment scan.

#### 4.2. Vertical Alignment of SiPM & Scintillator

To measure the time resolution at various vertical alignment configurations the scintillator remained

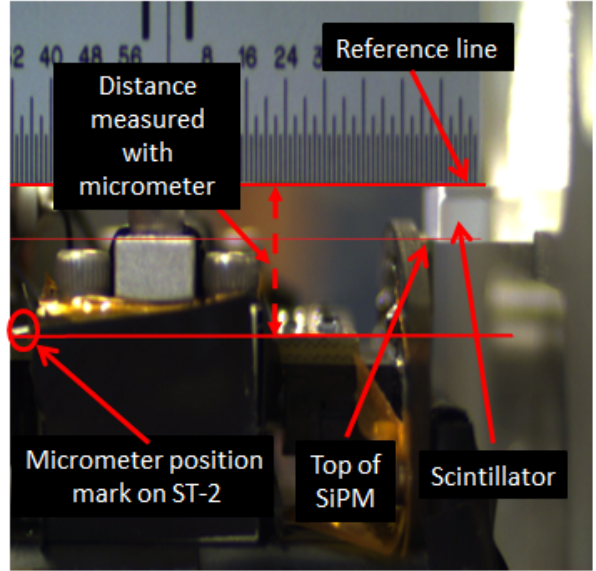


Figure 17: Vertical alignment optics set-up. The reference line corresponds to the top surface of the scintillator, while the micrometer position on the ST2 is clearly marked so that the absolute difference could be measured both optically and manually with a micrometer.

fixed while the SiPM scanned across the upstream end of the scintillator. The SiPM was lowered to the minimum location governed by the range of the MT translation stage. This distance was measured to be  $y = -4 \text{ mm}$ .

“Coarse” measurements were then taken at half turn intervals (159  $\mu\text{m}$ ) until the maximum height of the MT translation stage was reached which was approximately  $y = +4 \text{ mm}$ . In order to conduct “precise” measurements the SiPM was lowered to  $y = -1 \text{ mm}$  and then the translation stage was moved in quarter turn intervals (79.5  $\mu\text{m}$ ) until it reached  $y = +1 \text{ mm}$ . The results of these measurements can be seen in Fig. 18. For each distinct location of the SiPM, the distance traversed was verified by a manual measurement made with a micrometer with 25  $\mu\text{m}$  precision.

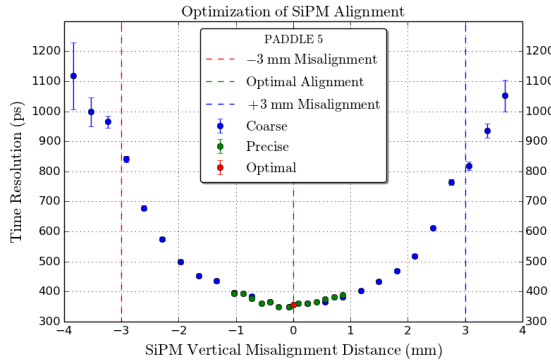


Figure 18: Coarse vertical misalignment results. The minimum time resolution obtained was approximately 350 ps which was expected. Once the SiPM exceeded  $y = \pm 3$  mm there is no active area of the SiPM coupled to the face of the scintillator.

From the vertical misalignment studies it is clear that there is no significant variation of time resolution within a  $\pm 300 \mu\text{m}$  range of the optimal alignment. These results were also simulated in a manner similar to what was discussed in section 3.2 and the results are seen in Fig. 19. The GEANT4 simu-

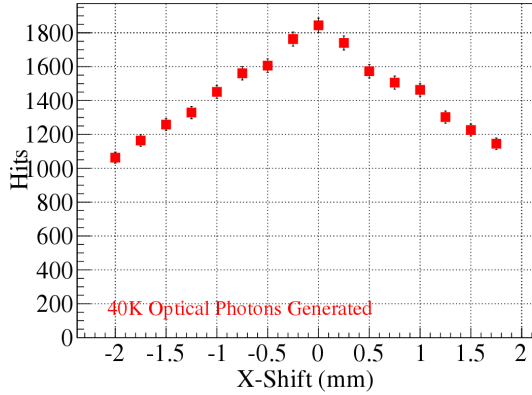


Figure 19: Vertical alignment simulation studies [14]. It is important to note the x-axis corresponds to the y-axis as discussed with the experimental measurements.

lations indicate that the acceptable range of vertical misalignment is approximately  $\pm 250 \mu\text{m}$  [14] which is consistent with what was measured on the bench.

#### 4.3. Coupling Distance of SiPM & Scintillator

With the vertical alignment between the scintillator and SiPM optimized, the effects of varying the coupling distance were also studied. Using an identical set-up as was described in section 4.2 the coupling distance, and resulting time resolutions, were measured at various locations with three distances shown in Fig. 20. While the coupling distance was

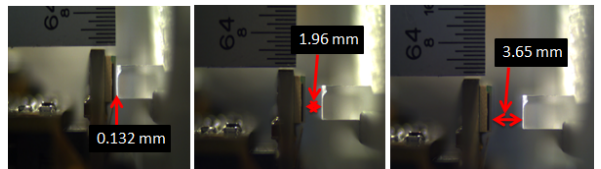


Figure 20: Various coupling distances as measured with the CMOS camera. The high degree of precision is clearly visible.

varied, the vertical alignment was kept constant at the optimal location and was monitored both optically and manually with a micrometer.

The SiPM was moved *via* the MT translation stage along the  $z$ -axis. We defined  $z = 0$  to be the instance when the active area of the SiPM was flush against the face of the machined scintillator paddle. In the coupling region  $z < 1$  mm the SiPM was receded from the face of the SiPM in 1/4 turn intervals ( $79.5 \mu\text{m}$ ). For  $1 \text{ mm} < z < 2$  mm, the SiPM was receded from the face of the SiPM in 1/2 turn intervals ( $159 \mu\text{m}$ ), and for  $2 \text{ mm} < z < 4$  mm data were collected in 1 turn intervals ( $318 \mu\text{m}$ ) with the results being illustrated in Fig. 21.

It is clear from the data the optimal coupling range was  $50 \mu\text{m} < z < 350 \mu\text{m}$  and there was no significant reduction in time resolution performance over a  $0 \mu\text{m} < z < 600 \mu\text{m}$  range. Similarly, the simulation results seen in Fig. 22 also indicate that

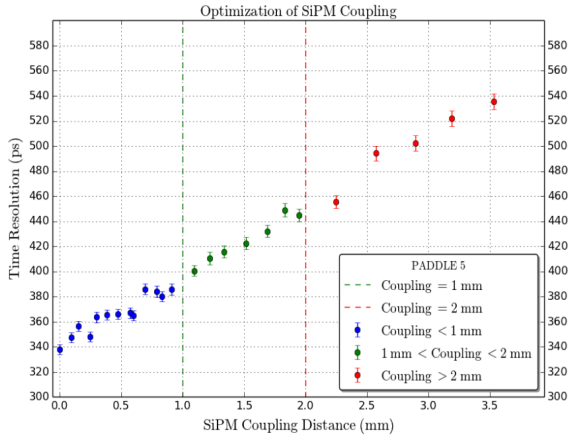


Figure 21: Coarse coupling distance studies. It is useful to note that at a coupling distance of  $251\ \mu\text{m}$  the time resolution was identical to what was measured in Fig. 18 while conducting the vertical alignment studies.

there is no significant reduction in light collection in the  $0\ \mu\text{m} < z < 600\ \mu\text{m}$  range [14].

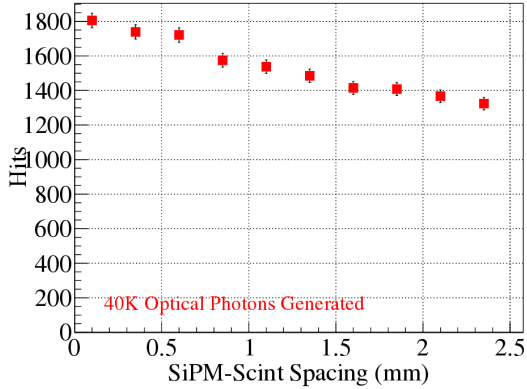


Figure 22: Coupling distance simulations. Simulations indicated that the optimal coupling distance is in the  $50\ \mu\text{m} < z < 350\ \mu\text{m}$  range.

## 5. Fabrication

In order to successfully identify the 2 ns electron beam bunch structure delivered by the CEBAF to within 99% accuracy, the GLUEX Start Counter time resolution is required to be  $< 350\ \text{ps}$ . In the

following section the details of polishing and characterizing machined scintillators, as well as the construction of the Start Counter are discussed.

### 5.1. Polishing Machined Scintillators

The surfaces of the machined scintillators incurred a plethora of surface defects and chemical contaminants known to harm scintillator surfaces while undergoing edge polishing at McNeil Enterprises. Therefore, in an effort to recover the scintillator surfaces and performance capabilities, polishing was required.

Prior to polishing the machined scintillators, a coarse measurement of the paddles performance was conducted to understand the magnitude of damage the paddles had incurred, relative to prototypes, as a result of mishandling. The time resolution and light output was measured at three precise locations along the length of the scintillators. One measurement was taken in the middle of the straight section, one in the middle of the bend, and one at the tip of the nose.

Figure 23 illustrates the erratic fluctuation and poor performance that existed from paddle to paddle prior to polishing. On average the 50 paddles did not meet the design resolution of 350 ps.

To polish the machined scintillator surfaces, Buehler Micropolish II deagglomerated  $0.3\ \mu\text{m}$  alumina suspension was utilized[15]. The polishing suspension was diluted with a 5:1 ratio of de-ionized  $\text{H}_2\text{O}$  to alumina and applied to a cold, wet  $6'' \times 0.5''$  Caswell Canton flannel buffering wheel[16] operated at  $< 1500$  RPMs. All surfaces of the scintillators were carefully buffed until all large, uniform surface defects were removed. In order to eliminate

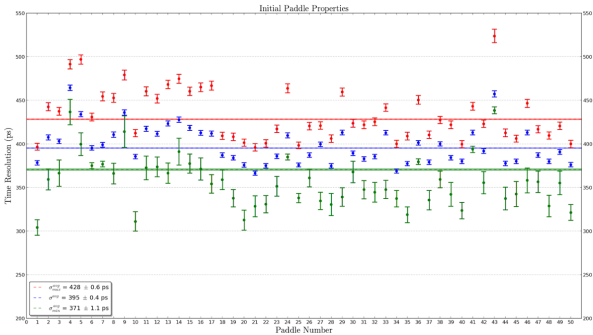


Figure 23: Coarse time resolution measurements prior to polishing. Paddle number is on the x-axis and time resolution in ns is on the y-axis. The red points are the resolutions in the bend region, the blue points are the weighted average of the three measurements, and the green points are the resolutions at the tip of the nose. The horizontal lines are the weighted averages of the individual measurements.

470 small, localized surface defects hand polishing with a soft NOVUS premium Polish Mate microfilament cloth[17] and diluted polishing suspension was applied. These polishing procedures made the scintillators void of virtually all scratches and surface 495 defects.

475 Once the appropriate polishing procedures had been developed and implemented the surface quality was greatly improved as can be seen in Fig. 24 which illustrates the same scintillator paddle before 480 and after polishing. A red laser beam was shone into the scintillator medium from the upstream end aimed at one edge so that the total internal reflection towards the tip of the nose was visible. The unpolished scintillator had such poor surface quality that the reflections in the bend region could not 485 be seen due to the multiple scattering of light at the scintillator boundaries. However, the reflections in the polished scintillator can clearly be seen traversing down through the nose region.

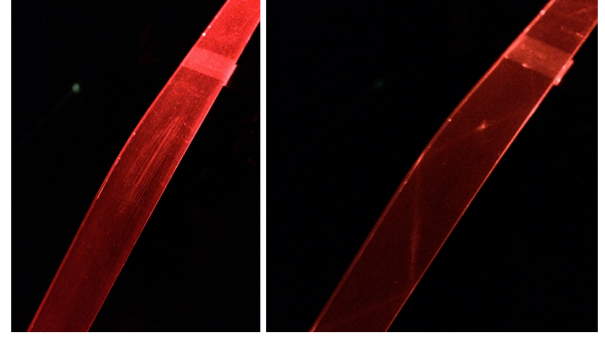


Figure 24: Effects of polishing scintillators. Left: non-diffuse laser incident on an edge, before polishing, at the upstream end of the straight section. Right: non-diffuse laser incident on the same edge, after polishing, at the upstream end of the straight section.

Once the scintillators were polished, their performance was remeasured so that a quantitative measure of the polishing effects were understood. The 490 measurements were performed in an identical manner outlined above and the pre-polished results were illustrated in Fig. 23. As expected, the time resolutions were greatly improved as seen in Fig. 25. On average, at the tip of the nose, the scintillators 495

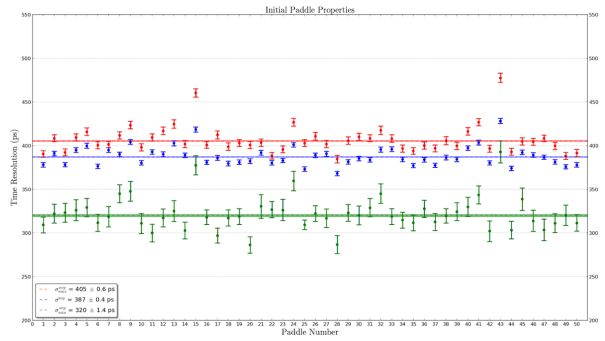


Figure 25: Coarse time resolution measurements after polishing. The details are identical to Fig. 23

exhibited a  $\approx 15\%$  improvement in time resolution. Moreover, there was a substantial reduction in erratic fluctuations in performance.

500 5.2. Testing Machined Scintillators

The polished machined scintillators were tested in order to measure their light output and time resolution properties. They were measured in an identical and reproducible manner utilizing a custom fabricated test stand shown in Fig. 26. The test

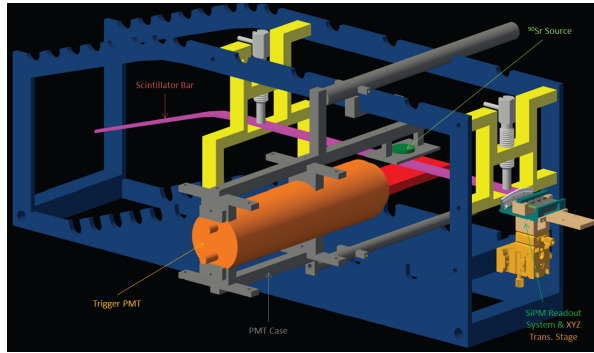


Figure 26: CAD Drawing of custom test stand.

505

stand facilitated the precise measurement of the aforementioned scintillator properties at 12 well-defined locations along the length of the scintillator paddles. Specifically 4 locations in the straight section, 3 in the bend, and 5 in the nose were tested.

The measurements were conducted with a collimated  $^{90}\text{Sr}$  source oriented orthogonal to the wide flat surface of the scintillators. The  $^{90}\text{Sr}$  source provided minimum ionizing electrons ranging in energy from 0.5 – 2.3 MeV *via* beta-decay [18][19]. A trigger Photo-Multiplier Tube (PMT) was placed underneath the scintillator on the opposite side of the  $^{90}\text{Sr}$  source and provided the TDC start time and ADC gate. A prototype SiPM detector identical to the SiPMs installed in the final ST assembly, was utilized to collect the light from the scintillators.

The analog signals from the SiPM and the trigger PMT were then processed through Nuclear Instrumentation Modules (NIM) so that both the ADC

525 and TDC spectra could be analyzed. The signal processing electronics diagram is illustrated in Fig. 27.

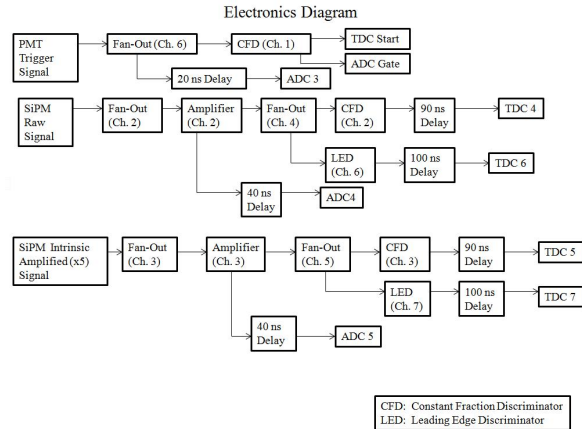


Figure 27: Electronics diagram for testing machined scintillators.

530 Utilizing a dedicated data acquisition computer configured with CEBAF Online Data Acquisition (CODA) software, 10,000 event triggers and associated data were collected at each of the locations along the scintillator path. Subsequently, the 535 ADC and TDC data were analyzed to measure the light output and time resolutions respectively of the whole lot of polished machined scintillators.

Once the 30 machined scintillator paddles which exhibited the best time resolution and light output properties from the lot of 50 were selected, they were carefully wrapped in Reynolds food grade aluminum foil. The aluminum foil is  $16.5 \mu\text{m}$  thick and possesses good reflectivity properties. Moreover, the aluminum foil protects the surfaces of the scintillators during both the testing and assembly processes.

540 The measured time resolutions for the 30 best scintillators, which comprise the ST, were found

to be satisfactory and even well below design resolution in the nose region which is illustrated in Fig. 28.

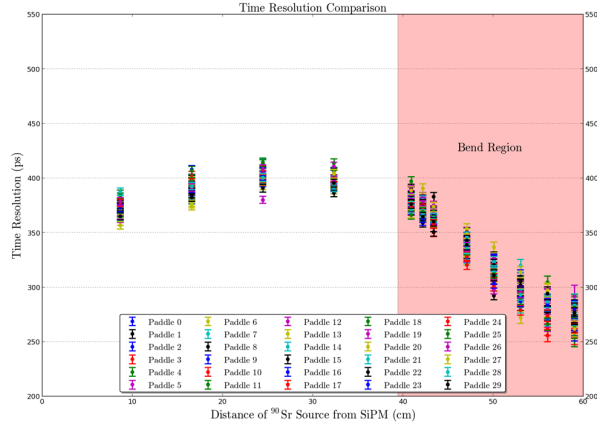


Figure 28: Time resolution of 30 the best scintillator paddles. The time resolution performance of the selected scintillators is remarkably similar while illustrating a spread of  $\approx 50$  ps in the nose region.

The unique geometry of the machined scintillator paddles exhibit a phenomenon of an increase in light collection in the nose region as the light source moves towards the tip at the downstream end. It is hypothesized that the relatively poor time resolution in the straight section is due to a reflective smearing effect in which light is able to traverse from the straight section down to the tip of the nose, and then back up to the upstream end.

The average time resolution of the individual scintillators selected for the final ST assembly are shown in Fig. 29.

### 5.3. Assembly

In order to assemble the ST an assembly jig, illustrated in Fig 30, was fabricated. The jig consisted of a rotating cylindrical mounting bracket rigidly attached to a 2" diameter shaft housed in

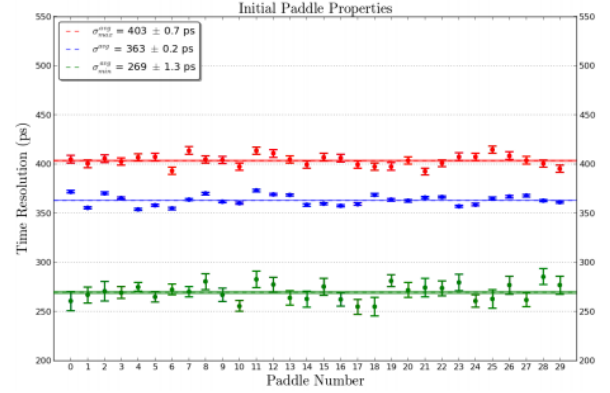


Figure 29: Average time resolution of 30 best scintillator paddles. The red data points correspond to the maximum time resolution obtained in all 12 data points. The blue data points are the weighted average of all 12 data points. The green data points indicate the minimum time resolution obtained in all 12 data points.

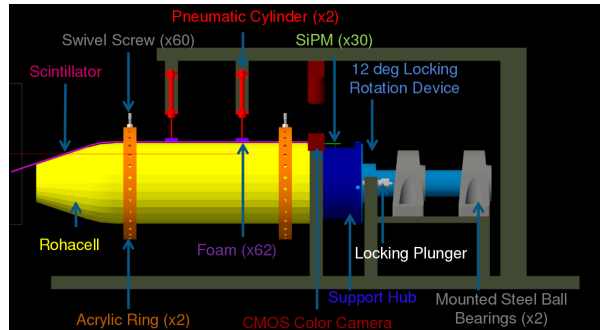


Figure 30: CAD drawing of the ST assembly jig.

two cast iron mounted steel ball bearings. The rotating bracket was engineered such that it was free to rotate unless engaged by a spring loaded locking plunger which would cause the assembly jig to move in discretized 12° intervals. This provided the ability to orient paddles parallel to the table top so that alignment and coupling could be performed reliably and reproducibly.

While mounted to the assembly jig, the upstream chassis (and Rohacell) was attached to the rotating bracket. A vertical bar running parallel to the ta-

ble above the Rohacell served as a mount for the 580 pneumatic cylinders so that the scintillators could be held firmly in place during installation. Furthermore, it provided a surface in which a portable flex arm could hold the CMOS camera to monitor the coupling of the scintillators and SiPMs.

A pressurized gas system was implemented to 585 provide manual control of the two pneumatic cylinders with soft, semi-dense rubber feet attached to the ends. The rubber feet would hold the scintillator being installed firmly in place by activating two switches which controlled each pneumatic 590 cylinder independently *via* bi-directional solenoids connected in a 5 psi nitrogen gas system.

Two free floating acrylic rings, with 30 tapped holes 12° apart, were fabricated so as to firmly hold the scintillator paddles in place during assembly. Each tapped hole housed a 10° swivel pad thumb 615

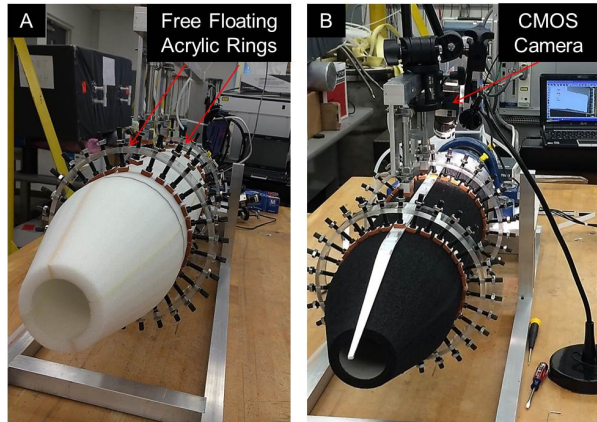


Figure 31: Free floating acrylic rings. Left: Rohacell prior to being painted with black latex paint. Each free floating ring is supported by 30 swivel pad screws. Right: Rohacell after being painted black. One wrapped scintillator paddle is being held firmly in place by two swivel pad screws.

595

screw which had silicone foam foot ( $0.25 \times 0.25 \text{ in}^2$ ) adhered to it in order to provide a soft barrier be-

tween swivel pad and the scintillator surface.

The camera and its associated software were utilized to measure scintillator/SiPM coupling distances and shimming heights with a precision of < 10  $\mu\text{m}$  in real time. The camera was calibrated such that at various magnification settings the distance to pixel ratio was known.

The 10 ST1 boards were mounted to the pre-fixed tapped holes along the lip of the upstream support hub. Black 1 mm spacers were installed between the ST1 PCB and the support hub to avoid any possibility of the electrical contact between the two.

The position of the ST1 was adjusted such that the distance between the top edge of the scintillator and the top edge of the active area of the SiPM was offset by 30 mils (762  $\mu\text{m}$ ). The offset was measured with the CMOS camera.

The paddle being installed was carefully positioned such that the upstream end was located approximately a millimeter away (downstream) from the active area of the SiPM and were held in place. A piece of 0.8 mil bundling wrap was wrapped firmly around the scintillator and the Rohacell structure as seen in Fig. 32. The distance between the top edge of the scintillator and the top edge of the active area of the SiPM was then measured in order to determine the amount of shimming necessary for radial alignment as illustrated in Fig. 33.

Three different thickness's (5, 10, 20 mil) of Kapton polyimide heavy duty film (type HN,  $\rho = 1.42 \text{ g/cm}^3$ ) were cut into  $0.5 \times 12 \text{ in}^2$  strips and utilized for shimming the scintillators in the radial direction. On average, each paddle required 30 mils of radial shimming.

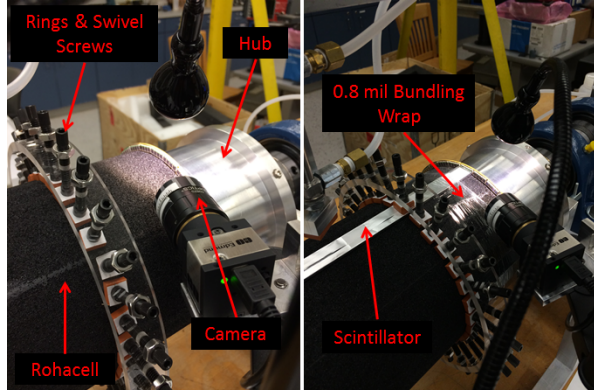


Figure 32: Aligning ST1 to support hub. Left: CMOS camera and lamp prepared to monitor ST1 positioning. Right: Reference scintillator wrapped to Rohacell during ST1 alignment.

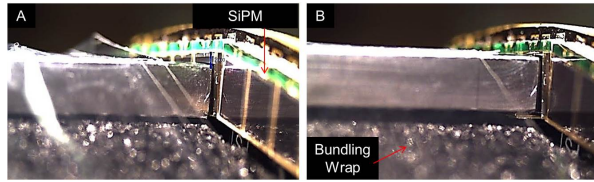


Figure 33: Shimming effects. Left: Before and Right: after shimming.

With the appropriate shimming in place, the paddle was carefully positioned such that the center of the upstream paddle was aligned with the center of the SiPM and the swivel screws were extended.  
635

A piece of computer paper sandwiched between two pieces of Al foil ( $\approx 150 \mu\text{m}$  thick) was then placed parallel to the active area of the SiPM and  
640 the paddle was then pressed firmly against the outer most piece of Al foil which is seen in Fig. 34. The piece of computer paper was carefully removed. Then, the Al foil pieces were removed individually so as to ensure no damage was incurred on the paddle surface or SiPM. Utilizing this method provided  
645 a coupling distance  $< 200 \mu\text{m}$ .

In order to make the ST light tight, an inner cone

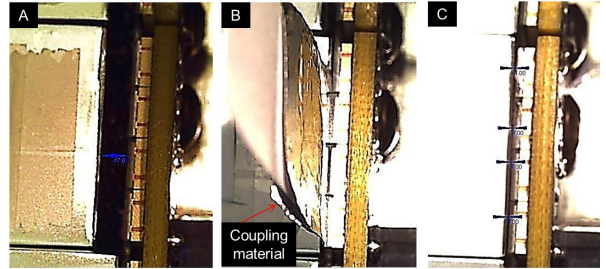


Figure 34: Steps of coupling paddles to SiPM. Left: Paddle prior to being coupled to SiPM. Center: Paddle pressed firmly against spacing material and SiPM. Right: Paddle properly coupled to SiPM at a distance of  $162 \mu\text{m}$ .

of black Tedlar polyvinyl fluoride  $\rho \approx 1.5 \text{ g/cm}^3$  [20] was taped to the Rohacell as seen in Fig. 35. A

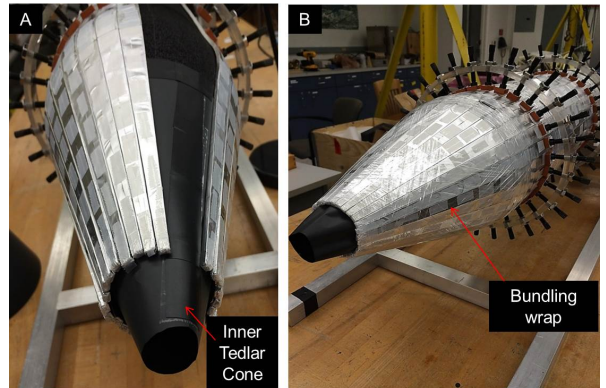


Figure 35: Inner Tedlar cone. Shown is before and after wrapping with bundling wrap. The cone was specifically engineered to have the same dimensions of the Rohacell support structure to avoid crumpling of the light tightening material.

few gaps existed in the Rohacell at the glue joints, and were filled in with black RTV silicone caulking. Moreover, it was painted with black latex paint for light tightening purposes.  
650

The support hub was also wrapped with Tedlar and taped down with black electrical tape. The spacing between the ST1 PCBs along with the bottom side of the support hub, was filled with RTV  
655

black opaque silicone caulking. Similarly, RTV silicone caulking was then applied to the inner edge 660 of the collar which encompassed the ST1 PCBs at their outer diameter.

In order to secure paddles to the Rohacell support structure the Start Counter was wrapped along its length using self-adhesive transparent bundling wrap (0.8 mil thick, 6 in wide) at six different locations 665 perpendicular to the central axis of rotation. Four locations were wrapped along the straight section at equal distance ( $\approx 8$  cm) from one another, one in the bend and one in the nose section. Five 670 layers of bundling wrap were applied to each section and the acrylic rings were removed as illustrated in Fig. 36.

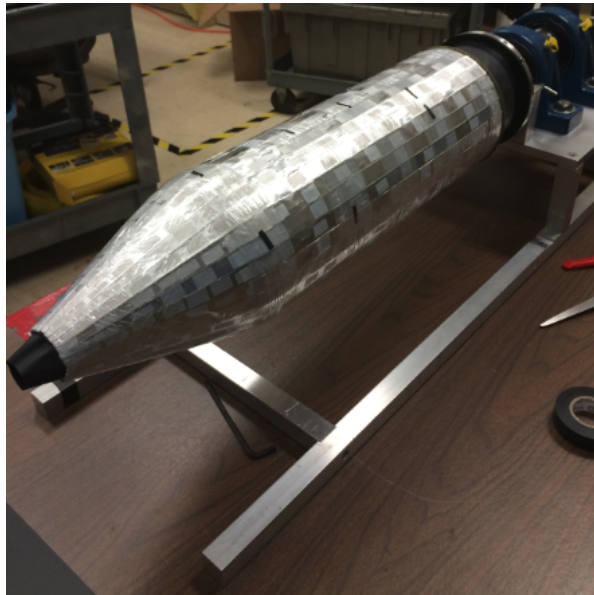


Figure 36: Isometric view of assembled Start Counter. The pieces are black electrical tape which mark the ends of 685 bundling wrap are clearly visible.

A cone of Tedlar was wrapped around the nose 690 region and taped down with electrical tape as seen in Fig. 37. The tips of the inner and outer cones in

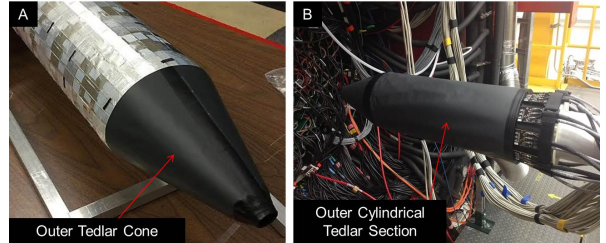


Figure 37: Light tight Start Counter. Left: Outer cone Tedlar piece. Right: Fully light tight Start Counter mounted to the Fall 2015 commissioning target.

the nose region were then taped together with electrical tape and trimmed of excess material. Furthermore, a cylindrical piece of Tedlar was taped down at the bend region and to the collar covering the ST1 boards. The fully assembled and cabled ST 680 mounted to the commissioning target can be seen in Fig. 37.

## 6. Calibration

In this section the various calibration procedures 685 taken in order to minimize the time resolution and enhance both the particle identification (PID) and time of flight (TOF) capabilities of the Start Counter are discussed.

### 6.1. Time-Walk Correction

The time-walk effect is a well understood consequence 690 of leading edge discriminators (LED). Analog signals of varying amplitudes crossing a fixed threshold, as determined by the discriminator threshold setting, will do so at varying times as illustrated in Fig. 38. Thus, the corresponding logic signal output from the LED will “*walk about*” in time, resulting in an undesirable smearing of the measured ST TDC times.

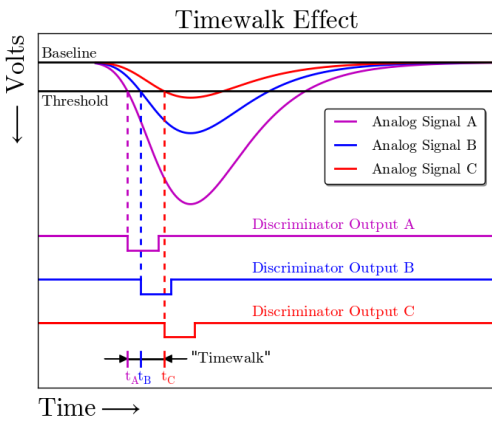


Figure 38: Example of the time-walk effect. Three coincident analog signals A, B, & C of varying amplitudes crossing a fixed threshold in a LED. The discriminator logic output signals vary in time relative to the amplitude of the incoming analog signal. The signals shown above are simulated analog signals being fed into the LED's thus, they have negative polarity.

The FADC250's provide a high resolution pulse time (62.5 ps) that is time-walk independent [1] [21]. Therefore, for events in which both the FADC and TDC register hits in the same channel, the pulse time can serve as a reference time for that event. The TDC/FADC time difference is given by Eq. 1.

$$\delta t_i = t_i^{TDC} - t_i^{FADC} \quad (1)$$

Figure 39 shows a typical time-walk spectrum, *i.e.*  $\delta t_i$  versus the pulse amplitude, for one sector of the ST. The FADC250's return both the amplitude and integral of events which are above threshold [21]. Since the amplitude better characterizes the ADC pulse profile as compared to the pulse integral, it was utilized for the time-walk corrections.

The non time-walk corrected spectrum illustrates the poor time resolution due to the large spread in time differences occurring among signals close to

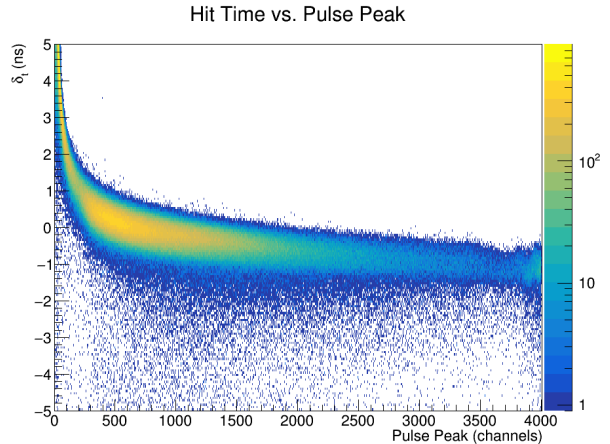


Figure 39: Typical Start Counter time-walk spectrum. Shown is the time-walk spectrum for sector 15 of the Start Counter during the Spring 2017 run. On the y-axis is  $\delta t_{15}$  and on the x-axis is the corresponding pedestal subtracted pulse peak spectrum. From this histogram it is clear that there is a correlation between the amplitude of the analog signal and the time in which the signal crosses the discriminator threshold.

threshold and the more probable amplitudes being registered in the FADC. From Fig. 39 it is immediately obvious that there exists a correlation between the time and the pulse peak for hits in the ST. This correlation is nonlinear and requires a polynomial functional form to describe the correlation. Equation 2 from reference [22] was chosen to characterize the correlation between  $\delta t_i$  and the amplitude of the signal.

$$f_i^w(a/a_i^{thresh}) = c0_i + \frac{c1_i}{(a/a_i^{thresh})^{c2_i}} \quad (2)$$

In Eq. 2  $f_i^w$  is the functional form of time-walk fit for the  $i^{th}$  sector, while  $a$  and  $a_i^{thresh}$  are the pulse peak and discriminator threshold converted to ADC units respectively. Furthermore,  $c0_i, c1_i, c2_i$  are the time-walk correction fit parameters.

The data in Fig. 39 were fit using Eq. 2 and ROOT's MINUIT  $\chi^2$  minimization fitting library

for pulse peak values ranging from [50, 2100]. An  
 735 identical fit was carried out for each of the ST sectors.

The most probable value (MPV) of the minimum ionizing peak was chosen to be the location in which  
 740 the time-walk correction was zero. This location effectively serves as a reference point for the correction. As seen in Fig. ?? a “pseudo” MPV was utilized. The “pseudo” MPV ( $a_i^0$ ) was determined on a  
 760

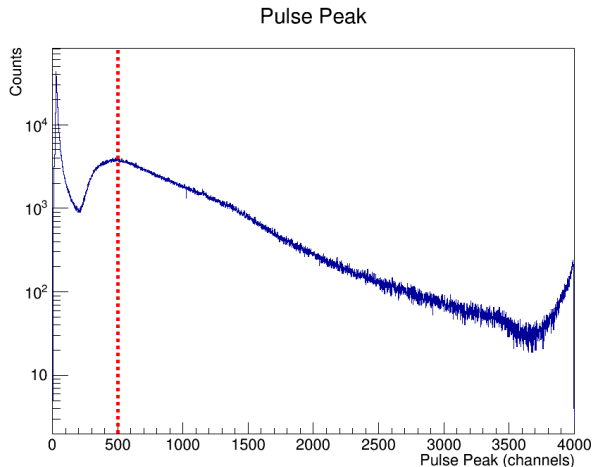


Figure 40: Typical pulse peak minimum ionizing distribution. Shown is the pulse peak minimum ionizing distribution for sector 3 during the Spring 2017 run. The red, vertical, dashed line in the histogram corresponds to the “pseudo” MPV ( $a_{15}^0$ ) which was determined to be 500.

sector by sector basis by simply acquiring the pulse peak channel which had the most number of entries  
 745 after the pulse peak channel 200. The large spike in the pulse peak spectrum at very low pulse peak values are due to electromagnetic background events clipping threshold and do not correspond to a true minimum ionizing particle traversing the scintillator medium.  
 750

With all the necessary parameters, *i.e.*  
 $a_i^0$ ,  $c0_i$ ,  $c1_i$ ,  $c2_i$ , determined the time-walk  
 770

correction factor can be applied to the original TDC time. The functional form of the time-walk corrected time is given by Eq. ??.

$$T_i^w = t_i^{TDC} - f_i^w(a/a_i^{thresh}) + f_i^w(a_i^0/a_i^{thresh}) \quad (3)$$

Once the time walk corrections have been applied, the corrected timing distributions appear much more uniform in nature and exhibit a factor 1.75 improvement in resolution [1]. Figure ?? illustrates the vast improvement in the time difference spectrum ( $\delta t_{15}$ ) due to the applied time-walk corrections. In Fig. ?? illustrates the  $\delta t_{15}$  distribution

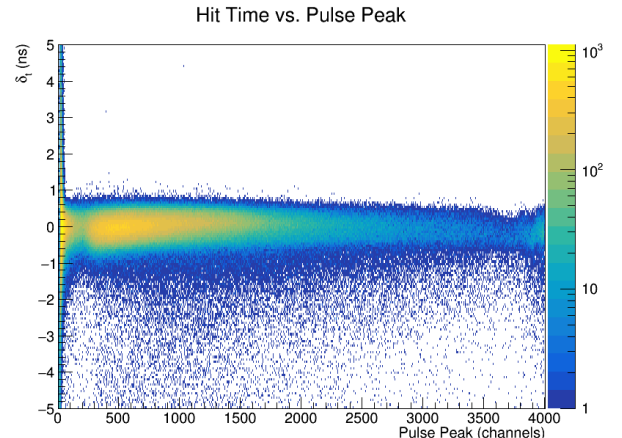


Figure 41: Time-walk corrected time difference spectrum. Shown is the time-walk corrected time difference spectrum for sector 3 during the Spring 2017 run. The time-walk corrected time difference spectrum has  $\sigma_{\delta t_{15}} \approx 270\text{ps}$

and the relative effects of the aforementioned time-walk correction.  
 765

## 7. Acknowledgments

The authors would like to graciously thank the plethora of Jefferson Lab staff members in both the Engineering division and Hall-D. Their numerous and invaluable contributions allowed for the Start

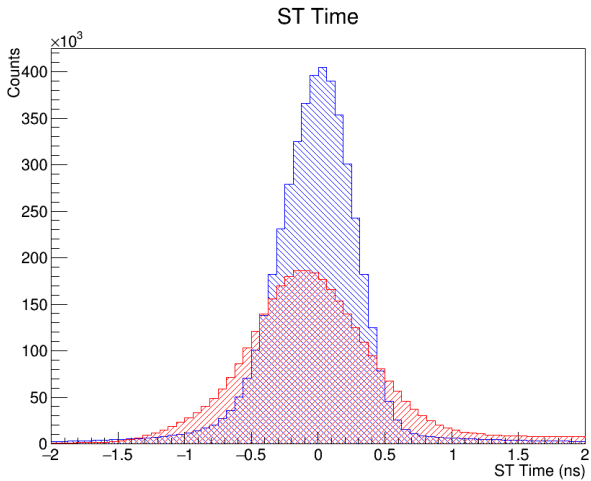


Figure 42: Comparison of pre and post self-timing distributions.

Counter project to come to fruition. The authors would also like to extend their gratitude to the entire GLUEX Collaboration who provided fruitful ideas and advice throughout the many stages of the 775 project. Work at Florida International University was supported in part by the Department of Energy under contracts DEFG0299ER41065 and DE-SC0013620. Furthermore, this material is based upon work supported by the U.S. Department of 780 Energy, Office of Science, Office of Nuclear Physics under Contract No. DE-AC05-06OR23177.

## References

- [1] E. Pooser, The GlueX start counter and beam asymmetry  $\Sigma$  in single  $\pi^0$  photoproduction, Ph.D. thesis, Florida International University (2016).
- [2] <http://www.eljentechnology.com/>.
- [3] General Purpose Plastic Scintillator EJ-200, EJ-204, EJ-208, EJ-212, technical note available at [http://www.eljentechnology.com/images/products/data\\_sheets/EJ-200\\_EJ-204\\_EJ-208\\_EJ-212.pdf](http://www.eljentechnology.com/images/products/data_sheets/EJ-200_EJ-204_EJ-208_EJ-212.pdf).
- [4] <http://www.rohacell.com>.
- [5] <http://www.mcnealplasticmachining.com/>.
- [6] <http://www.hamamatsu.com/us/en/index.html>.
- [7] Multi-Pixel Photon Counter, technical note available at [https://halldweb1.jlab.org/wiki/images/4/49/S10362-33\\_series\\_kapd1023e05.pdf](https://halldweb1.jlab.org/wiki/images/4/49/S10362-33_series_kapd1023e05.pdf).
- [8] <https://geant4.web.cern.ch/geant4/>.
- [9] K. S. Krane, Introductory Nuclear Physics, John Wiley & Sons, 1988, Ch. Detecting Nuclear Radiations, pp. 201–202.
- [10] C. M. Poole, A cad interface for geant4, paper submitted to Cornell Archive (arXiv) May 5, 2011 (2011). URL <http://arxiv.org/pdf/1105.0963.pdf>
- [11] A. L. . C. Moison, A more physical approach to model the surface treatment of scintillation counters and its implementation into detect, paper presented at IEEE, Nuclear Science Symposium; Anaheim, November 2-4 available at <http://geant4.slac.stanford.edu/UsersWorkshop/PDF/Peter/moisan.pdf> (1996).
- [12] P. Khetarpal, Start Counter Geant4 Simulations, start Counter Geant4 Simulations Wiki available at [https://halldweb.jlab.org/wiki/index.php/Start\\_Counter\\_Simulations](https://halldweb.jlab.org/wiki/index.php/Start_Counter_Simulations).
- [13] <https://www.newport.com/p/MT-XYZ>.
- [14] P. Khetarpal, Start counter: Optics simulations, talk Given at the February 16, 2012 GlueX Collaboration meeting (2012). URL [http://argus.phys.uregina.ca/gluex/DocDB/0019/001921/002/khetarpal\\_feb2012.pdf](http://argus.phys.uregina.ca/gluex/DocDB/0019/001921/002/khetarpal_feb2012.pdf)
- [15] <https://shop.buehler.com/consumables/grinding-polishing/polishing-suspensions/alumina-suspensions>.
- [16] <http://www.caswellplating.com/>

buffing-polishing/buffing-wheels/  
825 canton-flannel-wheels.html#.

[17] [https://www.novuspolish.com/polish\\_mates.html](https://www.novuspolish.com/polish_mates.html).

[18] <sup>90</sup>Sr Decay Radiation Data, national Nuclear Data Center, Nuclear Structure and Decay Database (NuDat) available at <http://www.nndc.bnl.gov/nudat2/decaysearchdirect.jsp?nuc=90SR&unc=nds>.

830 [19] <sup>90</sup>Y Decay Radiation Data, national Nuclear Data Center, Nuclear Structure and Decay Database (NuDat) available at <http://www.nndc.bnl.gov/nudat2/decaysearchdirect.jsp?nuc=90Y&unc=nds>.

835 [20] <http://www.dupont.com/products-and-services/membranes-films/pvf-films.html>.

[21] H. Dong, Description and instructions for the firmware of processing fpga of the adc250 boards version 0x0c0d, fADC250 Manual Available at [https://coda.jlab.org/drupal/system/files/pdfs/HardwareManual/fADC250/FADC250\\_Processing\\_FPGA\\_Firmware\\_ver\\_0x0C0D\\_Description\\_Instructions.pdf](https://coda.jlab.org/drupal/system/files/pdfs/HardwareManual/fADC250/FADC250_Processing_FPGA_Firmware_ver_0x0C0D_Description_Instructions.pdf) (February 2017).

840 [22] E. Smith, Low-level calibration constants for BCAL, technical note GlueX-doc-2618-v10, available at [http://argus.phys.uregina.ca/gluex/DocDB/0026/002618/010/bcal\\_constants.pdf](http://argus.phys.uregina.ca/gluex/DocDB/0026/002618/010/bcal_constants.pdf) (December 2014).

845